PHYSICS

Three-dimensional nonreciprocal transport in photonic topological heterostructure of arbitrary shape

Mudi Wang¹*, Ruo-Yang Zhang¹, Chenyu Zhang², Haoran Xue³, Hongwei Jia¹, Jing Hu¹, Dongyang Wang⁴, Tianshu Jiang², Che Ting Chan¹*

Electromagnetic wave propagation in three-dimensional (3D) space typically suffers omnidirectional scattering when encountering obstacles. In this study, we used Chern vectors to construct a topological heterostructure, where large-volume nonreciprocal topological transport in 3D is achieved. The shape of the cross section in the heterostructure can be arbitrary designed, and we experimentally observed the distinctive cross-shaped field pattern transport, nonreciprocal energy harvesting, and the remarkable ability of electromagnetic wave to traverse obstacles and abrupt structure changes without encountering reflections in 3D space.

Copyright © 2025 The Authors, some rights reserved; exclusive licensee American Association for the Advancement of Science. No claim to original U.S.
Government Works.
Distributed under a Creative Commons Attribution License 4.0 (CC BY).

Check for updates

INTRODUCTION

Topological materials have garnered notable attention from researchers due to their remarkable properties, in particular the unidirectional boundary transport (1-15), which makes them highly promising for applications such as optical communications, energy transport, and quantum computing. In comparison to two-dimensional (2D) systems, 3D topological materials offer greater degrees of freedom to control the propagation of waves, leading to a wide range of fascinating phenomena such as topological chiral Fermi arcs (16–19), negative refraction (20), Dirac-like surface states (21), antichiral surface states (22), 3D Chern insulators (23), and chiral Landau levels (24, 25). While the topological states are usually robust against defects and disorders, the existing methods only offer unidirectional transport in 1D edge or 2D surface of a topological material. The 3D nonreciprocal bulk transport is highly desired, but remains elusive, both experimentally and theoretically. Here, we propose an approach to realize highly robust 3D nonreciprocal bulk transport by designing topological heterostructures (26-30) of arbitrary shape. The embedded nontrivial Chern vectors ensure the immunity to obstacles and sharp boundary shapes, enabling efficient and unidirectional electromagnetic wave propagation in 3D space.

RESULTS

We consider a unit cell as shown in Fig. 1A, which consisted of the yttrium iron garnet (YIG) rod with the height $h_1 = 2$ mm and radius R, arranged on a metal plate with thickness $h_2 = 2$ mm in a hexagonal lattice array. The interlayer coupling strength is controlled by the circular holes with the radii of r = 2 mm (see more details in fig. S1). The lattice constant in the x-y plane is a = 16 mm, and the periodicity along z is h = 4 mm. The 3D structure exhibits "AA" stacking along the z axis, and the remaining space is filled with air. Figure 1B displays the corresponding first Brillouin zone (BZ). Crystals A and C

are subjected to a magnetic field of 0.1 T in opposite directions along the z axis, achieved by embedding the magnets beneath the YIG rods (R = 2 mm) within the metal plates. These magnetic crystals display the characteristics of 3D Chern insulators, exhibiting complete energy band gaps (the upper and lower panels of Fig. 1C). In contrast, the YIG rods (R = 1.65 mm) in crystal B remain unmagnetized and the crystal demonstrates properties of a nodal line semimetal, as depicted in the middle panel of Fig. 1C. By combining crystals A, B, and C in a heterostructure (Fig. 1D), which exhibits periodicity in the x and z directions, we observe the emergence of two sheets of distinct 3D waveguiding topological states (Fig. 1E), with the field distribution of the eigenstates spanning the entire 3D region of domain B. Within the frequency range (from 11.7 to 12.6 GHz) of topological nonreciprocal waveguide states (TNWSs), the slopes in the k_x direction at both valleys are positive for each fixed value of k_z , as shown in Fig. 1F, which exhibits one-way transport effects.

Before going further, we should develop the model Hamiltonians to understand the emergence of nonreciprocal waveguide modes in 3D space. The effective Hamiltonians describing domains A, B, and C around the valley near the Dirac points along the high-symmetry line K-H can be given as $H = k_x \sigma_x v_D - i \partial_y \sigma_y v_D + d_z^j \sigma_z$, where v_D represents the slope along both k_x and k_y directions, d_z^j (j = A, B, C) is a function of k_z to characterize the effective mass, and σ_i (i = x, y, z) denotes the Pauli matrices. The Hamiltonian form reflects the fact that the system is periodic along x and nonperiodic along the y direction (k_y is not a good quantum number). The band dispersion near the K-H valley is determined by the eigenvalue equation

$$H\psi = \delta\omega\psi\tag{1}$$

Domains A and C are 3D Chern insulators, characterized by the vectors of three Chern numbers $C_A = \left(C_x^A, C_y^A, C_z^A\right)$ and $C_C = \left(C_x^C, C_y^C, C_z^C\right)$, i.e., the Chern vectors (23). The model Hamiltonian gives $C_x^A = C_y^A = C_x^C = C_y^C = 0$, $C_z^A = \mathrm{sgn}(d_z^A) = -1$ and $C_z^C = \mathrm{sgn}(d_z^C) = 1$, while fig. S2 illustrates the results of full-wave simulation calculations for the Chern number. On the other hand, domain B carries the band dispersion of a typical nodal line semiconductor, which implies $d_z^B = 0$. In the heterostructure ABC, with domain B having a thickness denoted as L along the y direction, the A-B interface is positioned at y = L/2, while

¹Department of Physics, The Hong Kong University of Science and Technology, Hong Kong, China. ²MOE Key Laboratory of Advanced Micro-Structured Materials, Shanghai Frontiers Science Center of Digital Optics, Institute of Precision Optical Engineering, and School of Physics Science and Engineering, Tongji University, Shanghai 200092, China. ³Department of Physics, The Chinese University of Hong Kong, Shatin, Hong Kong SAR, China. ⁴Optoelectronics Research Centre, University of Southampton, Southampton SO17 1BJ, UK.

^{*}Corresponding author. Email: mudiwang@ust.hk (M.W.); phchan@ust.hk (C.T.C.)

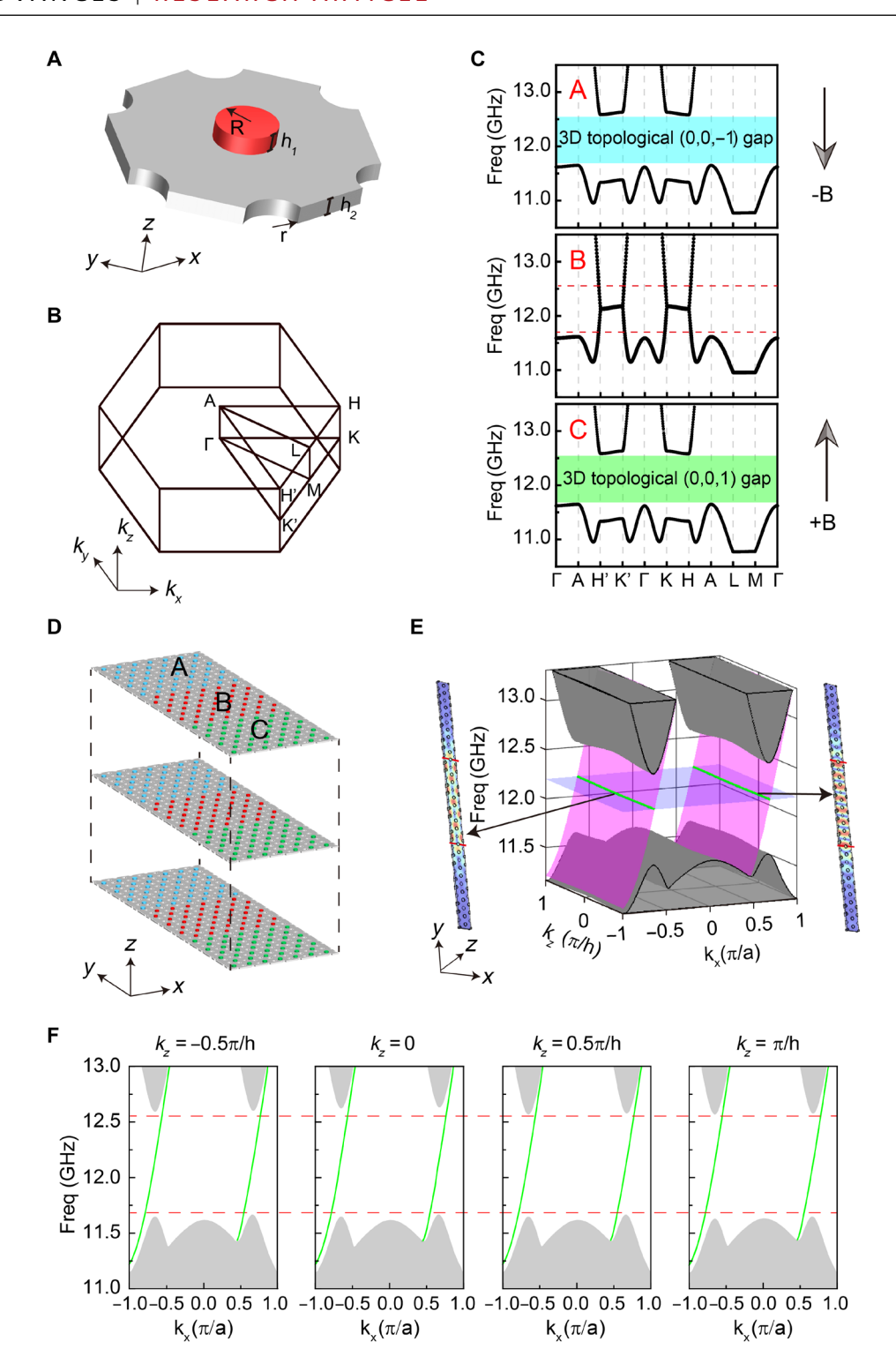


Fig. 1. Heterostructures for 3D TNWSs. (**A**) The unit cell of a gyromagnetic photonic crystal consisted of the YIG rod (red cylinder) and perforated metal plate (gray board). (**B**) Bulk Brillouin zone (BZ). (**C**) Band diagrams of the photonic crystal for crystals A, B, and C. In crystal A (C), the radius of YIG is r=2 mm, and it is subjected to a negative (positive) magnetic field B=0.1 T (B=-0.1 T). While in crystal B, the radius of YIG is R=1.65 mm, and there is no external magnetic field, hence B=0 T. (**D**) The schematic diagram of the 3D heterostructures consists of crystals A, B, and C. Each of these crystals, A, B, and C has a thickness of $\frac{7\sqrt{3}a}{2}$ along the y direction. (**E**) Band diagrams of the heterostructures. A frequency slice was plotted at 12.1 GHz, showing two intersecting green lines with the TNWSs. The illustration demonstrates two eigenstates at $k_z=0$. (**F**) The band dispersion of heterostructure ABC along the k_x direction at different k_z values.

the B-C interface is located at y=-L/2. For frequencies inside the band gaps of domains A (C), the nonreciprocal waveguide states in the heterostructure ABC are expected to exponentially attenuate along the positive (negative) y direction. The states can be described as $\psi_{\rm A}=\alpha_{\rm A}\varphi_{\rm k_A}e^{-u_{\rm k_A}\left(y-\frac{L}{2}\right)}e^{i(k_xx+k_zz)}$ and $\psi_{\rm C}=\alpha_c\varphi_{k_c}e^{u_{k_c}\left(y+\frac{L}{2}\right)}e^{i(k_xx+k_zz)}$. In domain B ($-L/2 \le y \le L/2$), the wave function can be expressed as the superposition of the two linearly independent bulk eigenstates at each k_x : $\psi_{\rm B}=\left(\alpha_{\rm B1}\varphi_{\rm k_B1}e^{-u_{k_{\rm B}}\left(y-\frac{L}{2}\right)}+\alpha_{\rm B2}\varphi_{\rm k_B}e^{u_{k_{\rm B}}\left(y+\frac{L}{2}\right)}\right)e^{i(k_xx+k_zz)}$. The coefficients $\alpha_{\rm A}$, $\alpha_{\rm Bp}\alpha_{\rm B2}$, and $\alpha_{\rm C}$ determine the amplitude of each superposed mode. Therefore, the nonreciprocal waveguide mode can be described as

$$\Psi_{ABC} = e^{i(k_{x}x + k_{z}z)} \begin{cases} \alpha_{A} \varphi_{k_{A}} e^{-u_{k_{A}} \left(y - \frac{L}{2}\right)}, y > \frac{L}{2} \\ \alpha_{B1} \varphi_{k_{B1}} e^{-u_{k_{B}} \left(y - \frac{L}{2}\right)} + \alpha_{B2} \varphi_{k_{B2}} e^{u_{k_{B}} \left(y + \frac{L}{2}\right)}, -\frac{L}{2} \le y \le \frac{L}{2} \end{cases} (2) \\ \alpha_{C} \varphi_{k_{C}} e^{u_{k_{C}} \left(y + \frac{L}{2}\right)}, y < -\frac{L}{2} \end{cases}$$

By considering the continuity of Eq. 2 at y = -L/2 and y = L/2, we can get the dispersion of the TNWS: $\delta \omega = k_x v_D$, while $u_{k_j} = \frac{|d_x^j|}{v_D}$ and ϕ_{k_A} , ϕ_{k_B} , ϕ_{k_B} , and ϕ_{k_C} are proportional to $\begin{pmatrix} 1 \\ -1 \end{pmatrix}$. Another TNWS thermore, it is essential for the transmission direction

of the waveguide modes at K'-H' valley to align with those at the K-H valley, as dictated by the Chern number difference ΔC_z of 2 between domains A and C. These TNWSs can be understood as a combination of the interface state at the A|C domain wall and the bulk states within domain B, resulting in bulk states with

nonreciprocal properties. It is important to note that crystal B cannot be arbitrary; it must be describable by the Hamiltonian mentioned above. In particular, domain B is domains A/C with time-reversal symmetry breaking turned off. In short, if domain B is a "gapped," the heterostructure supports two boundary modes that are localized at the interfaces between domains A/B and B/C, as shown in fig. S3. These modes exhibit exponential decay into domain B, due to its gapped nature. Meanwhile, as the width of domain B increases, the frequency range corresponding to TNWS will decrease, but this state will persist, as shown in fig. S4.

Now we proceed to the demonstration of 3D nonreciprocal transport. The top panel of Fig. 2A presents a photograph capturing a linear heterostructure, with copper-plated boards positioned at the bottom (fig. S5A) and top (fig. S5B). The top board features circular holes for the convenience of field measurements. The numerically computed (using COMSOL) isofrequency contours, represented by the green dashed line in Fig. 2B, appear as two nearly straight lines. To experimentally validate our findings, we conducted measurements on the xz plane within the domain B and performed 2D Fourier transform, generating the Fourier spectrum (the color map in Fig. 2B) in the momentum space. Figure 2C illustrates the field distribution in the heterostructure waveguide excited by a vertical line source under varying values of k_z , with periodicity observed in the z direction. Notably, the energy exhibits a uniform distribution across the entire domain B, indicating remarkable similarity in the field distribution as k_z varies. To evaluate the stability of the observed topological state, we introduced 20 aluminum cylinders with the same length as obstacles within the central region (the sample's photo is shown in the bottom panel of Fig. 2A), as depicted on the right side of Fig. 2C. We observed that the incident wave effectively circumvented these obstacles, allowing propagation

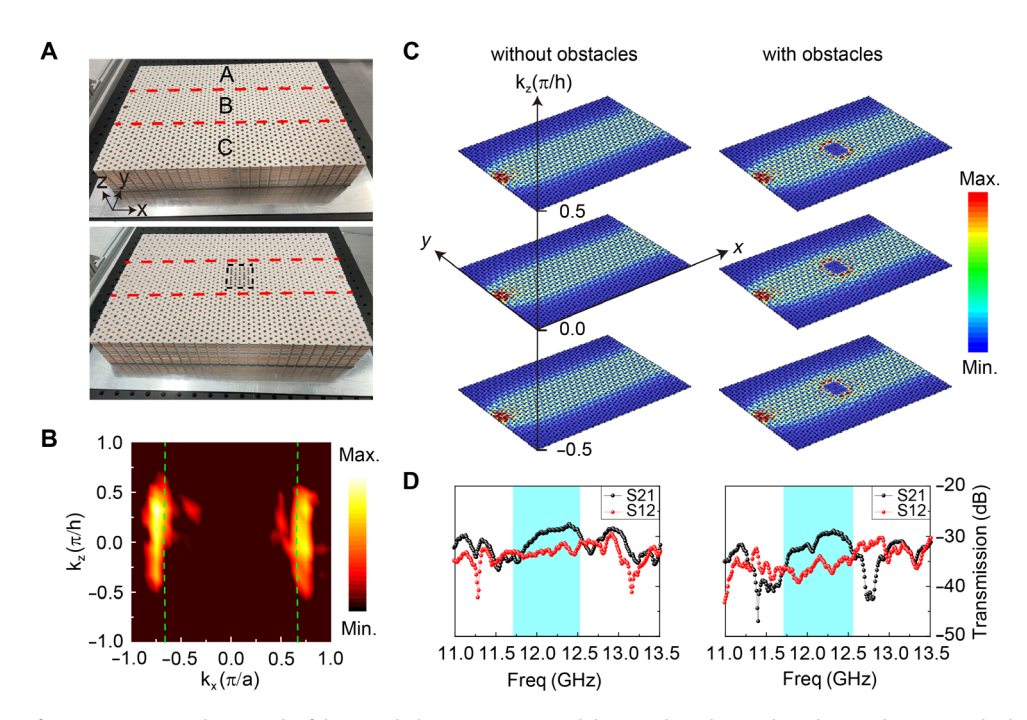


Fig. 2. Robust transport for 3D TNWSs. (A) Photograph of the straight heterostructure and the sample with PEC obstacles (20 aluminum cylinders are placed within the air holes of the black dashed rectangle). (**B**) Experimentally measured band structure (color map) compared with simulated result (green dash lines) at the $k_x k_z$ plane for 12.1 GHz. (**C**) The distribution of field with different k_z at 12.1 GHz for the normal structure and the structure with obstacles (20 aluminum cylinders). (**D**) Transmission coefficient S21 for the normal structure and the structure with obstacles.

with minimal disruption to the field distribution. We measured the transmission characteristics both in the absence and presence of 20 aluminum cylinders, as illustrated in Fig. 2D (see the Supplementary Materials for more details about the experimental measurement). The obtained results confirm the nonreciprocal nature of transport and its resilience to the presence of obstacles within the frequency range of TNWSs. In fig. S7, we also examined the scenario where 20 aluminum rods of varying heights act as obstacles, demonstrating that the nonreciprocity of TNWSs remains unaffected. In comparison to the 1D nonreciprocal edge states (10, 11), our study focuses on 3D waveguide states characterized by energy distribution across a significant 3D volume. The waveguide mode distributes energy almost uniformly across a large area in domain B. This feature is beneficial for certain applications, such as enhancing the mode's access to a larger gain region in lasing configurations. However, this even distribution can also lead to reduced signal intensity at specific measurement points. If domain B exhibits losses, the waveguide mode may encounter experimental losses while the energy from the incident point source remains constant, potentially resulting in diminished nonreciprocal characteristics.

The existence of TNWSs in 3D space opens up possibilities for controlling the bulk transport of electromagnetic waves by manipulating the shape of the heterostructure in different directions. We first focus on modifying the shape within the yz plane, which is perpendicular to the direction of wave propagation. Figure 3A provides a schematic representation of a cross-shaped heterostructure and the corresponding experimental sample. The heterostructure maintains periodicity along the x direction, while domain B takes on a cross shape in the yz plane. The projection of the band structure along the x direction for this cross-shaped heterostructure is illustrated by the green dashed lines in Fig. 3B. We should note that, there are a total of 15 distinct one-way bands in each valley, because there are 15 layers in the z direction. The bands within each valley are so closely spaced that they collectively appear as a single green line in Fig. 3B. This phenomenon can be understood using the model Hamiltonian analysis presented in the Supplementary Materials.

In the experiment, we conducted measurements along the *x* axis and applied a 1D fast Fourier transform to transform the collected data to momentum space. The resulting plot, depicted in the color map of Fig. 3B, demonstrates agreement with the corresponding theoretical predictions. The experimentally measured field distribution in the *yz* plane is presented in Fig. 3C, reveals an energy distribution taking the form of a cross shape. In comparison to the direct jointing of two different 3D Chern insulators (of opposite Chern vectors), the nonreciprocal waveguide states in the presented design can exhibit an arbitrary 2D field distribution perpendicular to the propagation direction as determined by the shape of domain B. More details can be found in fig. S8 to S11, and the corresponding supplementary text.

We proceed to modify the shape of the heterostructure in the xy plane (being periodic in the z direction), aiming to harvest input energy into a narrow region. Figure 3D provides a schematic illustration of the heterostructure configuration designed for this purpose and the corresponding experimental sample photo. In this particular configuration, domain B within the xy plane abruptly changes from a wide area (consisting of seven layers in the middle) to a narrow area (with zero layer in the middle, where domains A and C are in direct contact). Examining the simulated results after point source excitation at a frequency of 12.2 GHz with different k_z ,

Fig. 3E displays the field distribution where the energy concentrates from a larger area to a smaller area, effectively achieving the line focusing. In our experimental setup, we scanned the yz planes as indicated by the black dashed lines in Fig. 3D. Subsequently, we plotted the distribution of field intensity along the transverse y axis in Fig. 3F, where the contributions of different layers along the z direction were summed together. As anticipated, the experimental results indicate that during the transmission of microwaves along the x direction, the input energy can be effectively collected to the central region of y direction.

Last, we broke the periodicity of the sample in all x, y, and z directions. In this configuration, the domain B undergoes both bending and deformation, as illustrated in the top panel of Fig. 3G, with the experimental sample photo displayed in the bottom of it. The entire configuration retains its nonreciprocal bulk transport characteristics, since the topological properties of domains A, B, and C remain unaffected by the changes in configuration. On the other hand, the entire sample can also be viewed as multiple 2D yz sections being stacked along the x direction. As each individual section of heterostructure exhibits nonreciprocal effects, this property will remain valid for the whole structure.

In the experiment, we performed separate measurements of the transmission characteristics for a cross-shaped heterostructure (Fig. 3A), a focusing configuration (Fig. 3D), and a 90° curve configuration under deformation (Fig. 3G). The results, depicted in Fig. 3H, reveal a distinct nonreciprocity within the TNWSs region (highlighted by the blue shaded area). This observation demonstrates that despite variations in geometry, the nonreciprocal transport of electromagnetic waves in 3D space remains unaffected.

DISCUSSION

Our study demonstrates the nonreciprocal transport in 3D photonic heterostructures of arbitrary shape. This is achieved by incorporating a nodal line semimetal crystal between two distinct Chern insulators to form a heterostructure. Consequently, the initially reciprocal nodal line semimetal states undergo a transformative change, leading to the emergence of TNWSs. It is noteworthy that in the x direction, the heterostructure consistently exhibits nonreciprocity. In the yz cross section, electromagnetic waves will saturate the entire domain B and there is no nonreciprocity in directions normal to the x direction. This discovery establishes a platform for the effective control and manipulation of electromagnetic wave transport in 3D space.

MATERIALS AND METHODS

Numerical simulation

All theoretical simulations were performed using the radio-frequency module of COMSOL Multiphysics. In the calculation of the single-cell band structure shown in Fig. 1C, all directions were set as periodic. For the band calculations in Figs. 1 (E and F) and fig. S8, the x and z directions were set as periodic, while the remaining directions were set as scattering boundaries, removing the boundary states at the interfaces between domain A(C) and the scattering boundaries. In the calculation of the projected band structure in Fig. 3B, the x(z) direction was set as periodic (PEC), while the y direction was set as scattering boundaries, removing the boundary states at the interfaces between domain A (C) and the scattering boundaries.

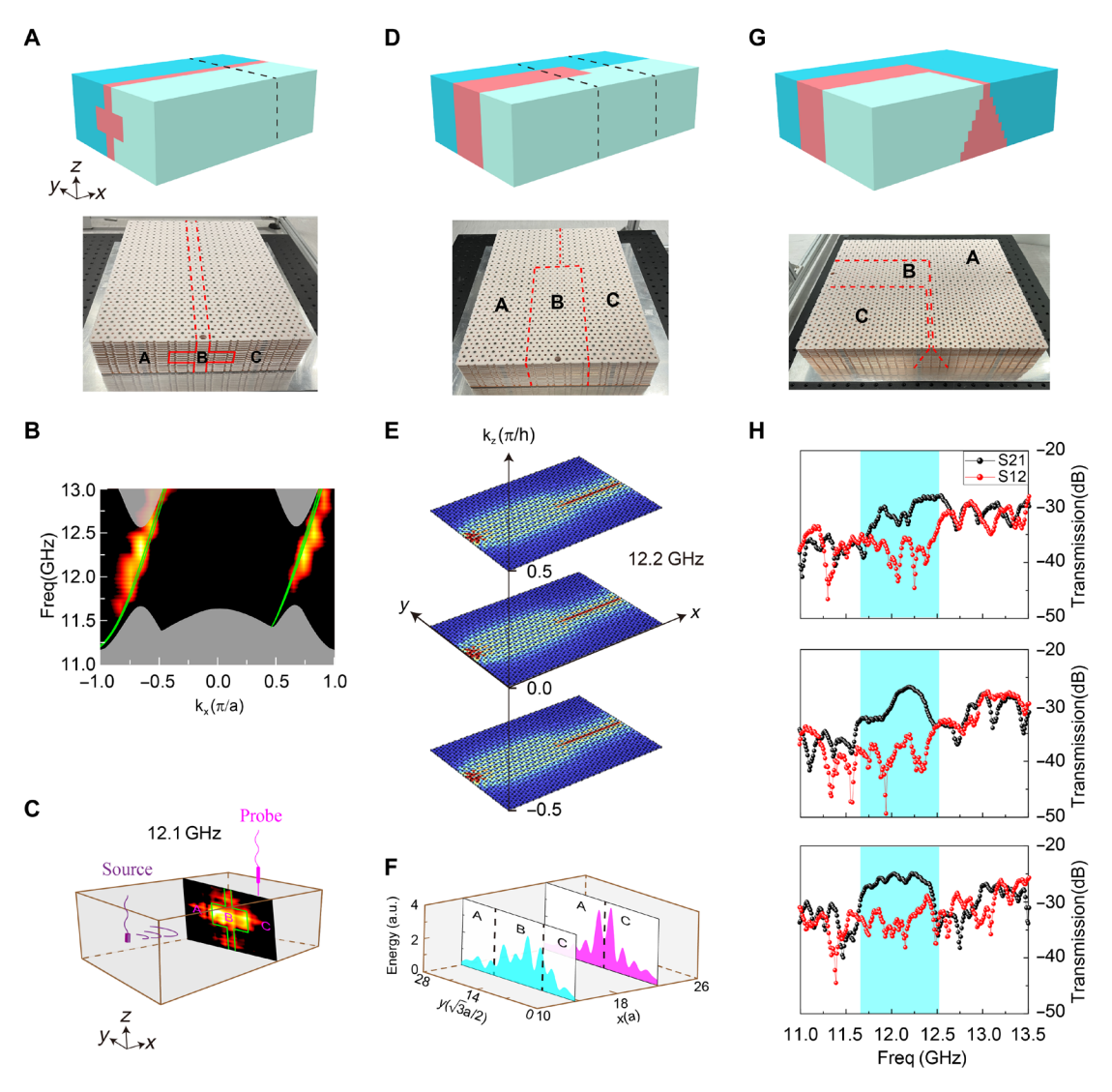


Fig. 3. Robust transport for 3D TNWSs with arbitrary shape. (A) Schematic diagram of a cross-shaped heterostructure and the corresponding experimental sample. (B) Experimentally measured projected band structure for the structure in (A), compared with the theoretical results. (C) Experimentally measured field distribution for the structure in (A) at 12.1 GHz. (D) Schematic diagram of a line-focused heterostructure and the corresponding experimental sample. (E) Simulated field distribution for the structure in (D) at 12.2 GHz with $k_z = -0.5\pi/a$, 0, and $0.5\pi/a$, with periodicity along the z direction. (F) Experimentally measured field intensity distribution with different y positions at planes X = 13a and X = 22a for the structure in (D). (G) Schematic diagram of 90° curve configuration while undergoing deformation and the corresponding experimental sample. (H) Transmission coefficients S12 and S21 for the structures in (A), (D), and (G).

The calculation of the Chern vector

Since the system is globally gapped, the Chern numbers for the \hat{x} , \hat{y} , and \hat{z} momentum planes can be well defined by $C_{x,y,z} = \frac{1}{2\pi} \int_{S^{x,y,z}} \Omega_n d^2k$, where $S^{x,y,z}$ represents the $k_{x,y,z}$ -fixed 2D section in the 3D BZ. Here, $\Omega_n(k) = \nabla_k \times A_n(k)$ is the Berry curvature, $A_n(k) = i \langle u_{n,k} | \nabla_k | u_{n,k} \rangle$ is the Berry connection and $u_{n,k}$ is the periodic part of Bloch state for the nth band. Moreover, fig. S2 displays the results of calculating the Chern number using full-wave simulations.

Materials and experimental setups

The YIG material parameters uses a saturation magnetization of $4\pi M_s = 1850$ G, a linewidth of $\Delta H = 50$ Oe, and a permittivity of

 $\epsilon = 13.8.$ A fully magnetized ferrite has a relative permeability tensor

in the form
$$\overline{\mu} = \begin{pmatrix} \mu & i\kappa & 0 \\ -i\kappa & \mu & 0 \\ 0 & 0 & 1 \end{pmatrix}$$
, where $\mu = 1 + \frac{\omega_m(\omega_0 + i\alpha\omega)}{(\omega_0 + i\alpha\omega)^2 - \omega^2}$ and

 $\kappa = \frac{\omega_m \omega}{\left(\omega_0 + i \alpha \omega\right)^2 - \omega^2}.$ The resonance frequency is denoted as $\omega_0 = \gamma H_{0P}$

where H_{0i} is the applied magnetic field (±0.1 T). The characteristic frequency as $\omega_m = 4\pi\gamma M_s$, and the gyromagnetic ratio as $\gamma = 2.8$ MHz/Oe.

On the copper-plated board, circular holes with a diameter of 3.2 mm are drilled at the positions of the YIG. Inside these holes, magnets with a diameter of 3 mm and a height of 2 mm are placed to

introduce the corresponding magnetic field in the desired direction. The YIG is held in place using thin-film boards with drilled holes (with a relative permittivity close to 1). The straight heterostructures, cross-shaped heterostructures, and line-focused heterostructures are composed of $26 \times 21 \times 15$ unit cells in the x, y, and z directions. While the 90° curve configuration while undergoing deformation consists of $26 \times 25 \times 15$ unit cells along the x, y, and z directions.

In the experimental setup, a vector network analyzer is used to connect both the source and probe antennas. By inserting the probe into the holes and scanning along the z direction, the field information inside the crystal is measured.

Supplementary Materials

This PDF file includes:

Supplementary Text Figs. S1 to S11

REFERENCES AND NOTES

- I. Martin, Y. M. Blanter, A. F. Morpurgo, Topological confinement in bilayer graphene. Phys. Rev. Lett. 100, 036804 (2008).
- F. Zhang, J. Jung, G. A. Fiete, Q. Niu, A. H. MacDonald, Spontaneous quantum Hall states in chirally stacked few-layer graphene systems. *Phys. Rev. Lett.* 106, 156801 (2011).
- L. Ju, Z. Shi, N. Nair, Y. Lv, C. Jin, J. Velasco Jr., C. Ojeda-Aristizabal, H. A. Bechtel, M. C. Martin, A. Zettl, J. Analytis, F. Wang, Topological valley transport at bilayer graphene domain walls. *Nature* 520, 650–655 (2015).
- J.-W. Dong, X.-D. Chen, H. Zhu, Y. Wang, X. Zhang, Valley photonic crystals for control of spin and topology. *Nat. Mater.* 16, 298–302 (2017).
- J. Noh, S. Huang, K. P. Chen, M. C. Rechtsman, Observation of photonic topological valley hall edge states. *Phys. Rev. Lett.* 120, 063902 (2018).
- Y. Ding, Y. Peng, Y. Zhu, X. Fan, J. Yang, B. Liang, X. Zhu, X. Wan, J. Cheng, Experimental demonstration of acoustic Chern insulators. *Phys. Rev. Lett.* 122, 014302 (2019).
- C. He, X. Ni, H. Ge, X.-C. Sun, Y.-B. Chen, M.-H. Lu, X.-P. Liu, Y.-F. Chen, Acoustic topological insulator and robust one-way sound transport. *Nat. Phys.* 12, 1124–1129 (2016).
- 8. J. Lu, C. Qiu, L. Ye, X. Fan, M. Ke, F. Zhang, Z. Liu, Observation of topological valley transport of sound in sonic crystals. *Nat. Phys.* **13**, 369–374 (2017).
- F. D. M. Haldane, Model for a quantum Hall effect without Landau levels: Condensedmatter realization of the "parity anomaly". Phys. Rev. Lett. 61, 2015–2018 (1988).
- Z. Wang, Y. Chong, J. D. Joannopoulos, M. Soljacić, Observation of unidirectional backscattering-immune topological electromagnetic states. *Nature* 461, 772–775 (2009).
- Y. Poo, R.-X. Wu, Z. Lin, Y. Yang, C. T. Chan, Experimental realization of self-guiding unidirectional electromagnetic edge states. *Phys. Rev. Lett.* 106, 093903 (2011).
- C.-Z. Chang, J. Zhang, X. Feng, J. Shen, Z. Zhang, M. Guo, K. Li, Y. Ou, P. Wei, L.-L. Wang, Z.-Q. Ji, Y. Feng, S. Ji, X. Chen, J. Jia, X. Dai, Z. Fang, S.-C. Zhang, K. He, Y. Wang, L. Lu, X.-C. Ma, Q.-K. Xue, Experimental observation of the quantum anomalous Hall effect in a magnetic topological insulator. *Science* 340, 167–170 (2013).
- Y. Deng, Y. Yu, M. Z. Shi, Z. Guo, Z. Xu, J. Wang, X. H. Chen, Y. Zhang, Quantum anomalous Hall effect in intrinsic magnetic topological insulator MnBi₂Te₄. Science 367, 895–900 (2020).
- Y.-F. Zhao, R. Zhang, R. Mei, L.-J. Zhou, H. Yi, Y.-Q. Zhang, J. Yu, R. Xiao, K. Wang, N. Samarth, M. H. W. Chan, C.-X. Liu, C.-Z. Chang, Tuning the Chern number in quantum anomalous Hall insulators. *Nature* 588, 419–423 (2020).
- M. Serlin, C. L. Tschirhart, H. Polshyn, Y. Zhang, J. Zhu, K. Watanabe, T. Taniguchi, L. Balents, A. F. Young, Intrinsic quantized anomalous Hall effect in a moiré heterostructure. Science 367, 900–903 (2020).

- X. Wan, A. M. Turner, A. Vishwanath, S. Y. Savrasov, Topological semimetal and Fermi-arc surface states in the electronic structure of pyrochlore iridates. *Phys. Rev. B* 83, 205101 (2011).
- S.-Y. Xu, I. Belopolski, N. Alidoust, M. Neupane, G. Bian, C. Zhang, R. Sankar, G. Chang, Z. Yuan, C.-C. Lee, S.-M. Huang, H. Zheng, J. Ma, D. S. Sanchez, B. Wang, A. Bansil, F. Chou, P. P. Shibayev, H. Lin, S. Jia, M. Z. Hasan, Discovery of a Weyl fermion semimetal and topological Fermi arcs. *Science* 349, 613–617 (2015).
- K. Deng, G. Wan, P. Deng, K. Zhang, S. Ding, E. Wang, M. Yan, H. Huang, H. Zhang, Z. Xu, J. Denlinger, A. Fedorov, H. Yang, W. Duan, H. Yao, Y. Wu, S. Fan, H. Zhang, X. Chen, S. Zhou, Experimental observation of topological Fermi arcs in type-II Weyl semimetal MoTe2. *Nat. Phys.* 12, 1105–1110 (2016).
- F. Li, X. Huang, J. Lu, J. Ma, Z. Liu, Weyl points and Fermi arcs in chiral phononic crystal. Nat. Phys. 14, 30–34 (2018).
- H. He, C. Qiu, L. Ye, X. Cai, X. Fan, M. Ke, F. Zhang, Z. Liu, Topological negative refraction of surface acoustic waves in a Weyl phononic crystal. *Nature* 560, 61–64 (2018).
- Y. Yang, Z. Gao, H. Xue, L. Zhang, M. He, Z. Yang, R. Singh, Y. Chong, B. Zhang, H. Chen, Realization of a three-dimensional photonic topological insulator. *Nature* 565, 622–626 (2019)
- X. Xi, B. Yan, L. Yang, Y. Meng, Z.-X. Zhu, J.-M. Chen, Z. Wang, P. Zhou, P. P. Shum, Y. Yang, H. Chen, S. Mandal, G.-G. Liu, B. Zhang, Z. Gao, Topological antichiral surface states in a magnetic Weyl photonic crystal. *Nat. Commun.* 14, 1991 (2023).
- G.-G. Liu, Z. Gao, Q. Wang, X. Xi, Y.-H. Hu, M. Wang, C. Liu, X. Lin, L. Deng, S. A. Yang, P. Zhou, Y. Yang, Y. Chong, B. Zhang, Topological Chern vectors in three-dimensional photonic crystals. *Nature* 609, 925–930 (2022).
- H. Jia, R. Zhang, W. Gao, Q. Guo, B. Yang, J. Hu, Y. Bi, Y. Xiang, C. Liu, S. Zhang, Observation
 of chiral zero mode in inhomogeneous three-dimensional Weyl metamaterials. *Science*363, 148–151 (2019).
- V. Peri, M. Serra-Garcia, R. Ilan, S. D. Huber, Axial-field-induced chiral channels in an acoustic Weyl system. Nat. Phys. 15, 357–361 (2019).
- S.-G. Cheng, J. Zhou, H. Jiang, Q.-F. Sun, The valley filter efficiency of monolayer graphene and bilayer graphene line defect model. *New J. Phys.* 18, 103024 (2016).
- M. Wang, R.-Y. Zhang, L. Zhang, D. Wang, Q. Guo, Z.-Q. Zhang, C. T. Chan, Topological one-way large-area waveguide states in magnetic photonic crystals. *Phys. Rev. Lett.* 126, 067401 (2021).
- M. Wang, W. Zhou, L. Bi, C. Qiu, M. Ke, Z. Liu, Valley-locked waveguide transport in acoustic heterostructures. *Nat. Commun.* 11, 3000 (2020).
- Q. Chen, L. Zhang, F. Chen, Q. Yan, R. Xi, H. Chen, Y. Yang, Photonic topological valley-locked waveguides. ACS Photonics 8, 1400–1406 (2021).
- J.-Q. Wang, Z.-D. Zhang, S.-Y. Yu, H. Ge, K.-F. Liu, T. Wu, X.-C. Sun, L. Liu, H.-Y. Chen, C. He, M.-H. Lu, Y.-F. Chen, Extended topological valley-locked surface acoustic waves. *Nat. Commun.* 13, 1324 (2022).

Acknowledgments

Funding: This work is supported by RGC Hong Kong through grants 16310420, 16307621, and AoE/P-502/20. D.W. acknowledges support from the Anniversary Fellowship of the University of Southampton. T.J. acknowledges support from the National Natural Science Foundation of China (12304345). H.X. acknowledges the support of the start-up fund from The Chinese University of Hong Kong. Author contributions: M.W. conceived the original idea, performed the simulations, and designed the samples. C.T.C. supervised the whole project. M.W., C.Z., and D.W. carried out the experiments. M.W. and R.-Y.Z. performed the analytical derivation. M.W., R.-Y.Z., H.X, H.J, J.H, D.W., T.J., and C.T.C. did the theoretical analysis. M.W., R.-Y.Z., and C.T.C. wrote the draft. All authors discussed the results and contributed to the manuscript.

Competing interests: The authors declare that they have no competing interest. Data and materials availability: All data needed to evaluate the conclusions in the paper are present in

Submitted 6 June 2024 Accepted 3 December 2024 Published 8 January 2025 10.1126/sciadv.adq9285

the paper and/or the Supplementary Materials.